Experimental Analysis of the Dynamics of Flared Folding Wingtips via a Novel Tethered Flight Test

Fintan Healy*, Alessandro Pontillo †, Djamel Rezgui‡ and Jonathan Cooper §
University of Bristol, Bristol, BS8 1TR, UK

James Kirk¶, Thomas Wilson‖ and Andrea Castrichini**
Airbus Operations Ltd, Bristol, BS34 7QQ, UK

Recent developments in morphing wing technologies are routinely tested using Unmanned Aerial vehicles (UAVs) due to their relatively low cost and time to manufacture. However, atmospheric flight tests limit both the repeatability of the recorded data sets, as well as the bounds of the flight envelope willing to be explored, due to the risk of destroying the UAV. In this paper, a novel flight test method is described, which consists of flying a UAV constrained by a tether, resulting in a steady, controlled, elliptical flight paths. The benefits of such a method are explored numerically to characterise the static and dynamic testing capabilities of such a system. This is then followed by an experimental investigation into the behaviour of semi-aeroelastic hinged (SAH) wingtips, employing the *AlbatrossOne* remotely piloted vehicle. The tethered model was used to explore the static effect of angle of attack and sideslip angle on the both the equilibrium position of the wingtips and the wingtips stability boundary.

I. Nomenclature

α = angle of attack
β = side-slip angle
Γ = circulation
ζ = damping
θ = fold angle
Λ = flare angle
ξ = polar angle
σ = cone angle
τ = UAV thrust magnitude; time constant
$\vec{F}$ = a force vector
F_y = the equivalent force at the centre of mass to produce the same moment about the root of the tether
f = frequency
g = acceleration due to gravity
h = tether length
X = force component tangential to the x axis in the body frame of reference
Y = force component tangential to the y axis in the body frame of reference
Z = force component tangential to the z axis in the body frame of reference
L = moment about the x axis in the body frame of reference
M = moment about the y axis in the body frame of reference
$\vec{M}$ = a moment vector
m = UAV mass

*PhD Student, Department of Aerospace Engineering.
†Research Associate, Department of Aerospace Engineering, MAIAA
‡Senior Lecturer, Department of Aerospace Engineering MAIAA.
§Airbus RAEng Sir George White Professor of Aerospace Engineering, Department of Aerospace Engineering, FAIAA
¶Airbus eXtra performance WING demonstrator - OAD - Performance & Mass Leader
‖Head of Technical Capability for Aircraft Loads, Flight Physics
**Loads and Aeroelastics Engineer, Flight Physics

N = moment about the z axis in the body frame of reference
q = generalised coordinates
V = velocity

II. Introduction

During flight an aircraft must operate over a range of flight conditions. However, wings are typically designed as a comprise, achieving sub-optimal performance in each condition. This comprise can by mitigated by the use of shape morphing technologies, which have received significant research interest in the last few decades [1, 2]. Historically, balancing the added cost, weight and complexity of such mechanisms with there benefits has limited there use to military applications. However, there has recently been a growing trend to develop such devices for small Unmanned Aerial Vehicles (UAVs) [1, 2], significantly reducing the lead time and associated cost in design, developing and testing morphing configurations.

When experimentally testing morphing configurations, the variation in static quantities (such as the lift over drag ratio) can be readily measured using wind tunnel models. However, measuring the effect of these devices on the dynamic behaviour of an aircraft, or developing control laws, can be a more challenging undertaking in a wind tunnel environment. A range of mounting strategies can be used to constrain the degrees of freedom of a model in a tunnel, with Huang and Wang [3] providing a good review of the subject. However, the size of the model is constrained by both the mounting strategy and the geometry of the working section. More-over the cost and relative scarcity of wind-tunnel time typically limits the amount of testing that can be conducted.

Therefore the free-flight testing of UAVs can be an attractive alternative. In such experiments a model can quickly be tested in multiple configurations, across a range of flight conditions in a relatively short period of time. However, the data collected from this form of testing is generally noisy in nature, with the model being exposed to wind, atmospheric turbulence and the weather. This can make rigorous scientific testing challenging due to the lack of a consistent and repeatable environment. Additionally, flight test programs are typically conservative in nature and do not push the bounds of the flight envelope. As the occurrence of any instabilities or adverse nonlinear behaviour could result in the loss of the entire aircraft, as happened to NASAs Helios prototype [4].

Another option is to fly a UAV whilst constraining some of its degrees of freedom. This can be achieved by attaching the UAV to a tether, rigidly mounted to the ceiling, constraining the UAV to a conical trajectory. This solution would retain many of the benefits of free flight testing, whilst also limiting the risk to the aircraft, and introducing a degree of consistency, allowing test variables to be controlled and easily compared. The adoption of tethers to constrain flying objects is not novel. It is in fact commonly used to fly tethered kites for wind power extraction at high altitude [5, 6]. The dynamics of flying vehicles constrained to a tether has commonalities with the free flying motion. However, coupling between longitudinal and lateral-directional dynamics is expected. Terink et al. [7] found that tethered kites show similarities in the longitudinal dynamics with regular kites, while the constraint introduced by the tether results in a more severe instability associated to the lateral motion. Also, derivation of the equations of motion for these UAVs can be found in Ref. [8, 9]. The novel method proposed in this paper presents strong similarities with the aforementioned studies. However, it simply aims to provide a stable and predictable trajectory for a UAV to obtain repeatable test results, rather than provide an energy recover mechanism.

Due to the significant moment arm between the root and tip of a wing, morphing wingtip devices have received considerable interest. The current research can generally be split into passive and active solutions, split across 3 major design motivations: control authority [10–12], optimising aircraft performance across different flight phases [13–16], and load alleviation [17–21]. Many of these devices can also be used to reduce the overall span of an aircraft on the ground, enabling next-generation aircraft configurations, which aim to reduce the lift-induced drag produced by an airframe by increasing the wingspan, to still use current airport infrastructure. With gate, runway and taxiway separations currently dictating the maximum span of aircraft [22, 23].

One such device, the Flared Folding Wingtip (FFWT) concept, has received significant research effort [17–20, 24–30]. As illustrated in Fig. 1, this device consists of a folding wingtip in which the hinge line has been rotated so that is is no longer parallel with the flow, with the angle denoted as the flare angle (Λ). In this configuration, an increase in the fold angle (θ) produces a decrease in the local Angle of Attack (AoA) of the wingtip, and vice versa in the other direction. Therefore, when an FFWT is free to rotate, the fold angle tends to an equilibrium position, defined as the coast angle, about which the aerodynamic and gravitational moments balance, and the system is statically stable [18].

The primary use of an FFWT is as a passive gust load alleviation device, with both experimental [18, 24] and numerical simulations [17, 19, 25] highlighting that significant reductions in the peak wing root bending stress can be

achieved during gust and manoeuvre loading, when compared to a fixed wingtip configuration. Further work has aimed to quantify the effect of FFWTs on the handling qualities [20] and roll performance [31] of an aircraft and previous flight tests have been conducted using the *AlbatrossOne* UAV [32], which is shown in Fig 2 and is the test structure considered within this paper.

This paper is structured into three sections. In the first, the AlbatrossOne model is introduced to provided a concrete example of a tethered flight test. In the second section, a set of numerical models are developed and then explored to understand the effect of the tether on both the static and dynamic properties of a UAV. Then, in the final section, the results from the AlbastrossOne test program are used to illustrate how both repeatable static and dynamic testing of a UAV can be achieved using the tethered configuration

III. The *AlbatrossOne* UAV

This work considers a series of tethered flight tests conducted using the *AlbatrossOne* small scale flight demonstrator, which is shown in Fig. 2. This UAV has been developed to test the FFWT concept in free flight. The result of initial flight tests were presented in [32], along with a detailed explanation of the manufacturing and onboard flight systems, which will not be reproduced here for brevity. In terms of instrumentation, *AlbatrossOne* was equipped with: an AoA vane, side-slip angle vane and pitot-static probe on the nose of the aircraft; onboard MEMs accelerometers and gyroscopes, and a camera situated in the vertical tailplane, which was used to measure the fold angle of both wingtips via a computer vision algorithm. Figure 2 indicates the location of both the AoA and side-slip vanes, as well as the camera. The wing of *AlbatrossOne* UAV is based on a generic short range aircraft, and is approximately 1:14 scale. The wing can be setup in one of three wingtip configurations:

1) A 2.6m wingspan with no wingtips.

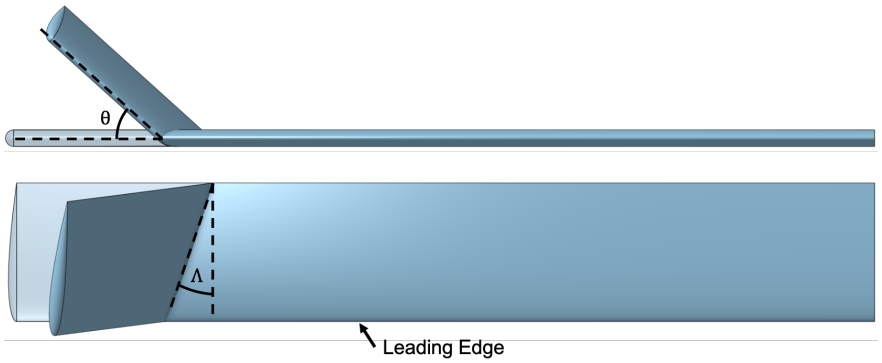

Fig. 1 Representation of a flared folding wingtip device, with a flare angle (Λ) of 20 degrees, at 0 and 45 degrees fold angle (θ)

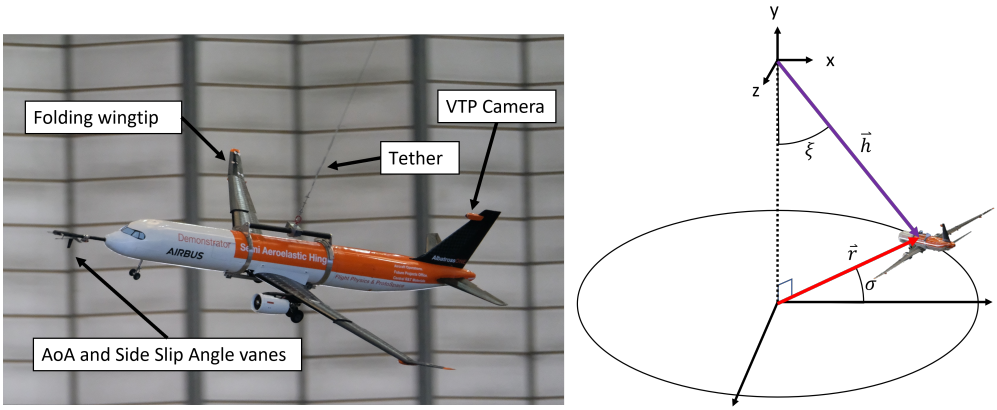

Fig. 2 Tethered flight test of the *AlbatrossOne* model. Copyright ©2021 Airbus

2) A 3.2m wingspan with FFWTs, with a flare angle of 17.5 degrees, connected via a Semi-Aeroelastic Hinge (SAH). This will be refereed to as the FWT32 configuration herein.
3) A 3.7m wing span with FFWTs, with a flare angle of 17.5 degrees, connected via a SAH. This will be refereed to as the FWT37 configuration herein.

A major upgrade to the *AlbatrossOne* model since [32] is the inclusion of a SAH. This device allows the wingtips to be either: in a "fixed state" where the wingtip is rigidly connected to the inner wing via an actuator (allowing the fold angle of the wingtips to be manually adjusted), or in a "free state" in which the wingtips are free to rotate about the hinges. A transition between these two states can be triggered at any point in a test by the pilot, allowing the *AlbatrossOne* model to simulate all aspects of a gate-to-gate flight. In which the aircraft starts at an airport gate with the wingtips folded up, taxi's to the runway and deploys the wingtips prior to flight*. It is envisaged that the wingtip would typically be locked in flight for optimal cruise performance, whilst unlocked during manoeuvres and gust encounters to alter the dynamic behaviour and reduce peak wing loading.

A series of flight test were performed in the Brabazon Hanger on the Airbus Filton site in which the UAV was tethered to the ceiling via a 23 metre cable. The primary aims of these tests were to:

1) understand the effect of angle of attack and side slip angle on the coast angle of the FFWTs, up to and beyond the boundary on stability.
2) test the dynamic release and retrieval of an FFWT in flight, and assess its effect on the pitching behaviour of the UAV
3) assess the potential relationship between the constrained and unconstrained aircraft longitudinal and lateral flight dynamics.

For each test, the UAV was launched by somebody running with it in a circular motion, at which point the pilot engaged the motors and proceeded to fly the UAV in a cyclic trajectory, at a target velocity.

Additionally, between the model and the tether was a "roll cage" which could be either "locked" or "free". In the "locked" state the roll angle of the UAV relative to the tether was fixed, and in the "free" state it allowed the UAV to roll by ±30 degrees under the tether, as shown in Fig. 3.

IV. Tethered Flight Test - Numerical Modelling

To explore the static a dynamic properties of an aircraft constrained to a tether, the Equations of Motion (EoM) of a simplified five Degrees of Freedom (DoF) system were developed. As shown in Fig. 2 the tether is analogous to a spherical pendulum, and as such can be defined by: the length of the tether, h; the polar angle, ξ; and the azimuthal angle, σ, which will be referred to as the cone angle herein. Two reference frames can be defined at the end of the tether,

*A video of an example gate-to-gate flight can be viewed at `https://youtu.be/R9SRn5n7enQ` [Accessed: 20/10/2021]

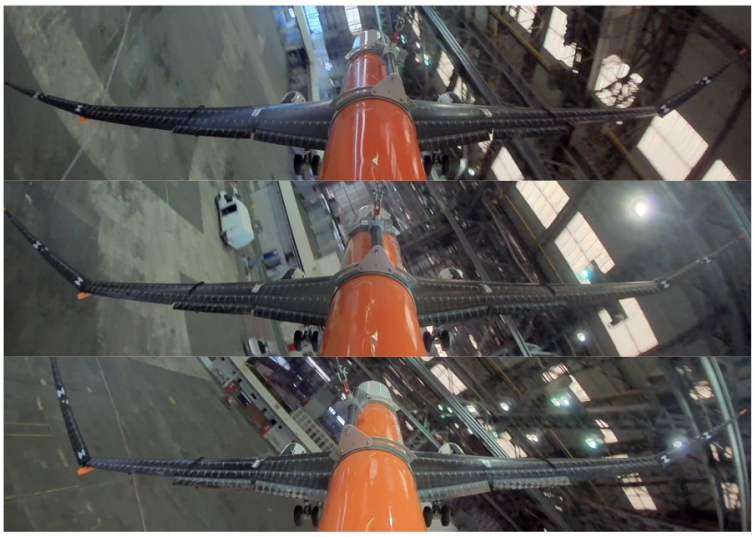

Fig. 3 Images of the UAV rolling underneath the tether. Copyright ©2021 Airbus

the first is the tether reference frame, in which the z axis is co-linear with the tether, pointing away from the origin, and the direction of the x axis is defined by the vector cross product $\vec{r} \times \vec{h}$, as shown in Fig. 2. The second is the body reference frame of the aircraft, in which the x axis points out of the nose of the aircraft, within the plane of symmetry of the aircraft, a z axis perpendicular to the x axis, and also in the plane of symmetry of the aircraft, and a y axis points out along the starboard wing of the UAV.

The origin of both the body and tether references frame is at the Centre of Mass (CoM) of the UAV. The rotation from the tether to the body reference frame is defined using an XZY Euler angle set (μ, β, α). In the case where the velocity of the aircraft is parallel to the x axis of the tether frame, these angles represent the bank angle, yaw angle and angle of attack of the model respectively, and when combined with the polar and cone angle, define the generalised coordinates of the system

$$\vec{q} = \left[\xi, \sigma, \mu, \beta, \phi\right]^T \tag{1}$$

The mass and moments of inertia of the aircraft (m, I_{xx}, I_{yy}, I_{zz}) are defined in the body reference frame and the external forces and moments applied to the UAV (such as aerodynamic forces, which will be derived in the next section) are defined by the two vectors

$$\vec{F} = \left[X + \tau, Y, Z\right]^T \qquad \vec{M} = \left[L, M, N\right]^T \tag{2}$$

where X, Y and Z are the axial, lateral and normal aerodynamic force components in the body reference frame; L, M and N are the rolling, pitching and yawing moments; and τ is the thrust of the UAV, which will be assumed to point along the x axis of the body reference frame. To simplify the EoM it was assumed that the effect of the pitch and yawing moments on the polar and cone angles (ξ and σ respectively), as well as there derivatives, is small.

An exact form of the EoM of this system were found using the Euler-Lagrange method, utilising the python packages moyra[†] and sympy [33], and were of the form

$$\mathbf{M}\left(\mathbf{q}, \dot{\mathbf{q}}\right) \ddot{\mathbf{q}} - \vec{f}\left(\mathbf{q}, \dot{\mathbf{q}}\right) = \vec{g}\left(\mathbf{q}, \dot{\mathbf{q}}\right) \tag{3}$$

where $\mathbf{M}$ is the mass matrix, $\vec{f}$ is a vector of conservative forces and $\vec{g}$ is a vector of external forces. The full form of these terms is shown in appendix A. Using a similar process, a second set of EoM were developed to describe an aircraft in free flight, with the generalised coordinates

$$\vec{q}_{\text{ff}} = \left[x, y, z, \mu, \beta, \phi\right]^T \tag{4}$$

where the symbols x, y and z represent the location of the origin of the body frame of reference in the global coordinate system.

A. Aerodynamic Model

The aerodynamic forces acting on the AlbatrossOne UAV were modelled using the Vortex Lattice Method (VLM) [34]. In which the main wing and empennage were discretised into a number of vortex ring panels, with a trailing horseshoe vortex appended to each ring on the trailing edge to satisfy the Kutta condition. The rings of the main wing were oriented such that the setting angle and jig-shape were accounted for, additionally, the camber of the main wing was accounted for by applying a uniform rotation to the panels equal in magnitude to the 2D zero-lift-angle of the chosen airfoil profile.

It is important to realise that the flow field observed from the body frame of reference of the aircraft may be non-uniform. for example, for a non-zero cone angle, if a UAV is travelling at a constant angular rate ($\dot{\xi}$), then the parts of the UAV further away from the centre of rotation will be rotating faster than parts closer in. To capture this effect an expression was developed to describe the velocity vector, $\vec{v}$ at a given position, $\vec{x}$ in the body reference frame

$$\vec{v} = \mathrm{v}_{\text{body}}(\vec{x}, \vec{q}, \dot{\vec{q}}) \tag{5}$$

the derivation of which is described in appendix B. This vector represents the local velocity vector at an arbitrary point in the body reference frame as a function of the generalised coordinates and there first derivatives with respect to time.

[†]https://pypi.org/project/moyra/ [Accessed: 27/10/2021]

It can therefore be used to define the boundary conditions at each panel within the VLM, allowing the aerodynamic forces to be calculated for any value of $\vec{q}$ and $\dot{\vec{q}}$.

The forces and moments about the centre of mass due to the aerodynamic forces were calculated by summing up the contributions of each vortex segment, using the vector form of the Joukowski theorem [34]

$$\vec{F}_i = p\Gamma_i \left(\vec{U}_i \times \delta\vec{l}_i\right) \tag{6}$$

$$\vec{F} = \sum_{i=0}^{N} \vec{F}_i \tag{7}$$

$$\vec{M} = \sum_{i=0}^{N} \vec{r}_i \times \vec{F}_i \tag{8}$$

where Γ_i is the circulation around the i'th vortex segment $\delta\vec{l}_i$, $\vec{r}_i$ is the displacement between the centre of mass and the i'th vortex segment, $\vec{U}_i$ is the total velocity at the i'th vortex segment, and N is the total number of vortex segments.

V. Numerical Results

A. Static Testing

One of the primary benefits of tethered flight testing compared to free flight testing is the ability to create repeatable trajectories in which flight parameters such as the velocity, AoA and side slip angle can be varied individually. Consider the case in which a tethered UAV is flown at a constant cone angle, attitude and velocity. In this condition the EoM reduce to two algebraic expressions

$$0 = h\left(-Y\sin(\beta) + Z\sin(\alpha)\cos(\beta) + (X+\tau)\cos(\alpha)\cos(\beta)\right)\sin(\sigma) \tag{9}$$

$$\begin{aligned} 0 =& ghm\sin(\sigma) - h^2 m\sin(\sigma)\cos(\sigma)\dot{\xi}^2 - hY\cos(\beta)\cos(\mu) \\ &+ hZ\left(\sin(\alpha)\sin(\beta)\cos(\mu) - \sin(\mu)\cos(\alpha)\right) + (X+\tau)\left(\sin(\alpha)\sin(\mu) + \sin(\beta)\cos(\alpha)\cos(\mu)\right) \\ =& ghm\sin(\sigma) - h^2 m\sin(\sigma)\cos(\sigma)\dot{\xi}^2 + hF_y \end{aligned} \tag{10}$$

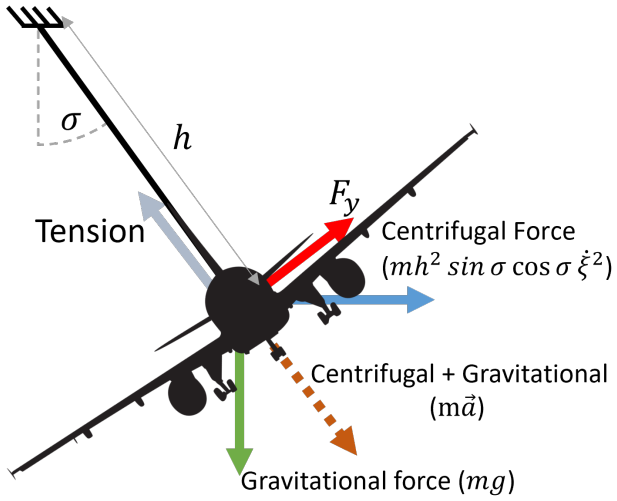

Fig. 4 A representation of the forces acting on a tethered UAV, in the non-inertial reference frame of the aircraft

where h is the length of the tether and g is the acceleration due to gravity. Eqn. (9) is simply the statement that the sum of forces in the direction of travel must equal zero. By rearranging Eqn. (9) we can find an expression for the required thrust for a given constant-cone-angle manoeuvre

$$\tau = -X + \frac{Y \tan(\beta)}{\cos(\alpha)} - Z \tan(\alpha) \tag{11}$$

Eqn. (10) is the summation of torques acting about the rotation axis of the cone angle. With the first term representing the torque due to gravitational forces, the second the torque due to centrifugal forces and the rest the torque due to aerodynamic forces acting on the UAV, which can be rewritten as hF_y, where F_y represents an equivalent force acting through the CoM, perpendicular to the tether. These forces can also been seen diagrammatically in Fig. 4. Eqn. (10) indicates that in a constant-cone-angle manoeuvre there is a relationship between the rate of change of the polar angle, $\dot{\xi}$, and the cone angle, σ. By considering how the local horizontal velocity of the aircraft (V) is related to the rate of change of the polar angle

$$\dot{\psi} = \frac{V}{h \sin\sigma} \tag{12}$$

Equation (10) can be rearranged as

$$V = \sqrt{\frac{h\left(-F_y + gm\sin(\sigma)\right)\tan(\sigma)}{m}} \tag{13}$$

This relationship is shown in Fig. 5 for a range of tether lengths, at a bank and side slip angle of zero degrees. As a typical tether test is envisaged to occur indoors, operational cone angles will be some value below 80 degrees (to avoid hitting the ceiling). Therefore, the length of tether needs to be selected based on the desired flight velocities and the facilities available to user. The different tether lengths in Fig. 5 represent different scenarios; a two metre tether would be achievable in most buildings, and would allow for flight speeds up to approximately $7ms^{-1}$ to be tested; a ten metre tether would be achievable in most sports halls suited for national competitions and would allow for flight speeds up to approximately $20ms^{-1}$; and a 23 metre tether (such as achieved in the Brabazon Hanger) would allow for test speeds up around $30ms^{-1}$.

In addition to increasing the cone angle, increasing the velocity in a constant-cone-angle manoeuvre also increases the magnitude of the combined inertial forces experienced at the CoM of the aircraft (the summation of gravitational and centrifugal forces)

$$m\vec{a} = \begin{bmatrix} 0 \\ \frac{mV^2}{h} \\ mg \end{bmatrix} = \begin{bmatrix} 0 \\ (-F_y + mg\sin\sigma)\sin\sigma\tan\sigma \\ mg \end{bmatrix} \tag{14}$$

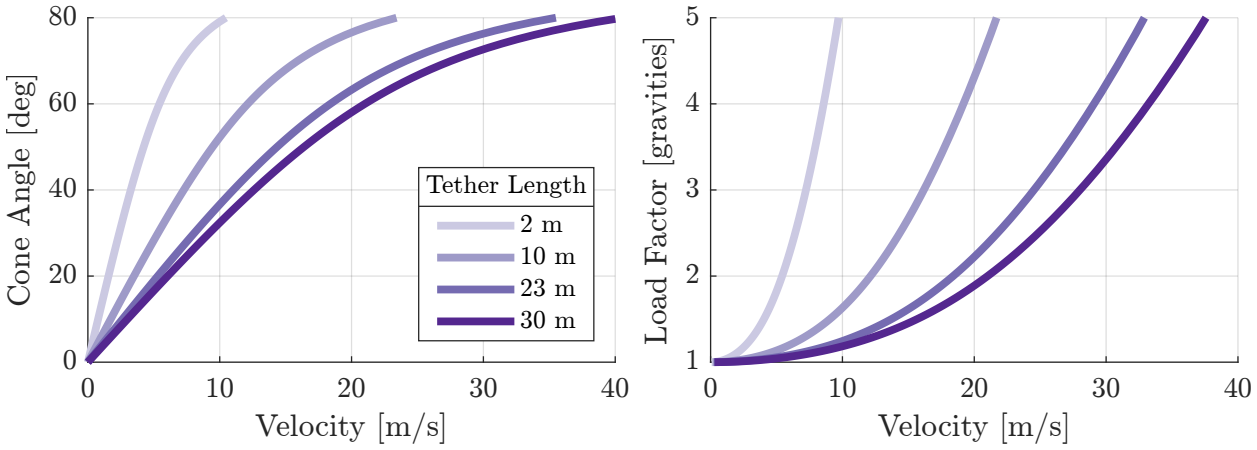

Fig. 5 The variation in the cone angle and load factor for a constant-cone-angle manoeuvre at varying velocities and tether lengths, for a bank and side slip angle of zero degrees

where $\vec{a}$ is the effective acceleration vector experienced by the aircraft. How the magnitude of $\vec{a}$ varies with velocity is shown in Fig. 5. Firstly, note how Eqn. (14) is independent of the length of the tether, h. Therefore the local acceleration of a UAV is only dependent on the cone angle. Secondly, consider the case where F_y tends to zero, in such a condition $\vec{a}$ must be co-linear with the tension in the tether. Therefore, in the body frame of reference, a constant-cone-angle manoeuvre is somewhat analogous to a coordinated turn.

To understand how the cone angle and local acceleration vector vary with attitude during a constant-cone-angle manoeuvre, an iterative process was used coupling the AlbatrossOne VLM model (including fuselage) described in section IV.A with the EoM of a tethered aircraft (Eqn. (3)). For a given flight velocity, AoA, side slip and bank angle, a minimisation routine was used to find the cone angle and thrust force required to ensure $\ddot{\vec{q}} = \dot{phi} = \vec{0}$ in Eqn. (3). As shown in in Figs. 6 & 7, this process was executed across a range of velocities, AoAs and side slip angles. Figure 6 shows that the cone angle and load factor are almost independent of the AoA, which can be explained by considering the balance of forces about the CoM of the UAV, as shown in Fig. 4. The tension in the tether is not a constant, instead it can 'adapt' to balance the forces acting through the CoM, therefore as long as there is some positive tension in the tether, tension and lift can be exchanged by changing the AoA of the UAV. Hence, when constrained to a tether, a UAV can be flown at multiple AoAs at the same velocity and cone angle.

Figure 7 shows that the cone angle and load factor vary linearly with side slip angle. This effect is primarily due to the change in F_y from two sources. Firstly, at increased side slip angles the fuselage and vertical tail plane produce increasing amount of side force, and secondly, at non-zero side slip angles the thrust vector has a component that directly contributes to side-force. The magnitude of the thrust vector also increases with side slip angle to compensate for both the reduction in the component of thrust in the x direction, and due to the increase in induced drag from the fuselage and vertical tail plane. It should also be noted that the magnitude of these variations with side slip angle will be highly dependent on the model being tested, and even Fig. 7 is likely to have under predicted the variations for the AlbatrossOne model, due to the omission of any sources of drag other than induced drag. However, Fig. 7 highlights that during static testing the maximum cone angle will be achieved at positive side slip angles, which will most likely define the maximum speed at which a model can be tested.

In Figs. 6 & 7, the term "Grav. Angle" represents the angle between where the local acceleration vector, $\vec{a}$, would point in a coordinated turn, and the actual acceleration vector experienced on the tether. It therefore represents how closely the loading of a constant-cone-angle manoeuvre represents that of a coordinated turn. Such considerations would be particularly important when testing flexible UAVs, as changes in this value will change how the structure deforms under load.

Another important consideration when operating a UAV whilst constrained to a tether is the effect of flow curvature. As the UAV travels through a circular path the flow field observed from the body frame of reference becomes curved. This variation in velocity is described by Eqn. (5), which is derived in appendix B. This curvature has been visualised for two constant-cone-angle manoeuvres in Figs. 8 & 9, using the AlbatrossOne model as a example. These figures show a variation in the flight velocity of $\sim 5\%$ from tip to tip as well as significant variations in both the AoA (~ 8 deg) and side slip angle (~ 4 deg) between the nose and tail of the UAV. Furthermore, the magnitude of these variations will be a function of the cone angle. Considering the two extreme cone angles at a constant polar rate, $\dot{\xi}$. Firstly, at a cone angle of zero degrees the UAV will spin about its z axis, meaning there will be zero change in the AoA and a 180 degree change in side slip angle nose-to-tail. Secondly, at a cone angle of 90 degrees the UAV will rotate about an axis parallel to the y axis in the body frame of reference. Therefore, there will be zero change in side slip angle and a large change in the AoA nose-to-tail. At cone angles between these two extremes there will be a sliding scale as to whether the flow field is dominated by a change in the local AoA or side slip angle nose-to-tail.

These variations in the local flow field direction present both operational and experimental challenges. From an operational standing, to ensure the aircraft can be trimmed in pitch during flight, either a large elevator angle must be achievable, or the setting angle of the empanage must be adjusted to a negative angle. Additionally, the location of flow measurement devices, such as the turning vanes and pitot-static probe at the nose of AlbatrossOne in Fig. 2, must be accounted for when accessing the attitude of the model.

From an experimental perspective, this can lead to asymmetries between measurements on either side of the model, and the location of any points of interest must be accounted for to ensure the correct local flow conditions are predicted.

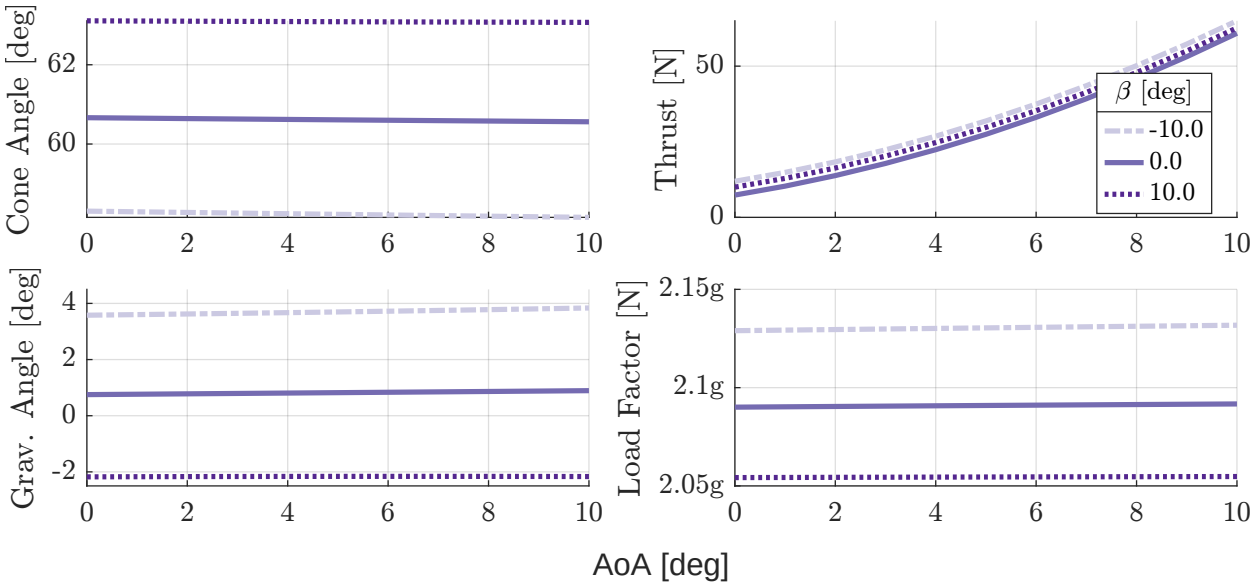

Fig. 6 The variation in the the cone angle and load factor with side slip angle, for a circular trajectory at a multiple velocities and AoAs, at a tether length of 23 metres

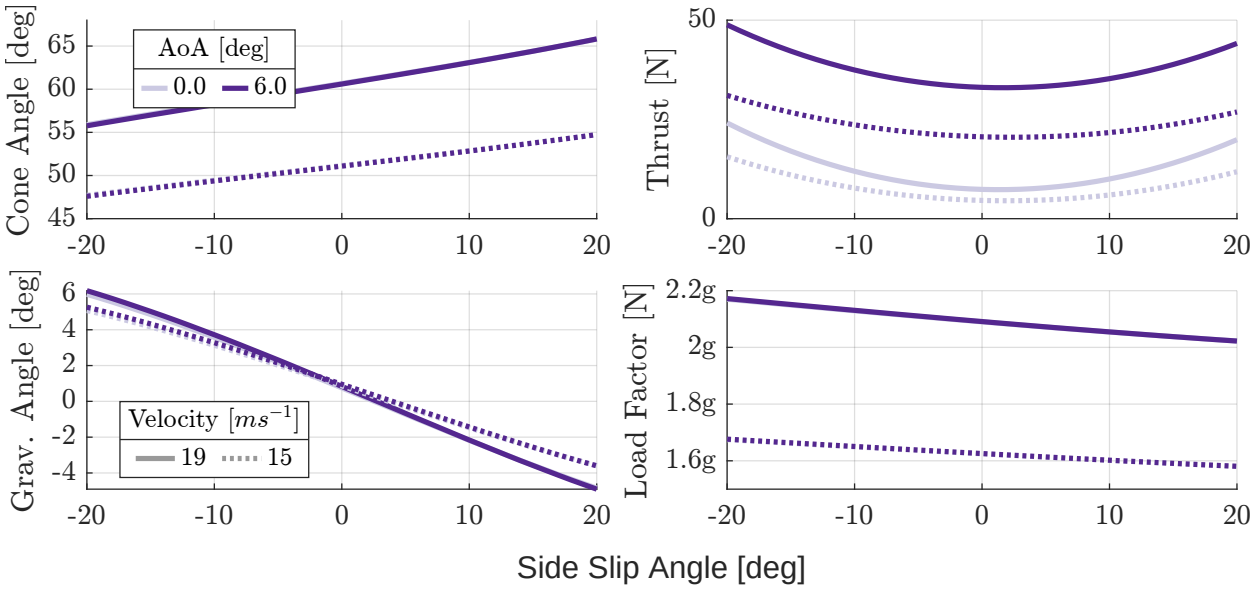

Fig. 7 The variation in the the cone angle and load factor with AoA, for a circular trajectory at a multiple velocities and side slip angles, at a tether length of 23 metres

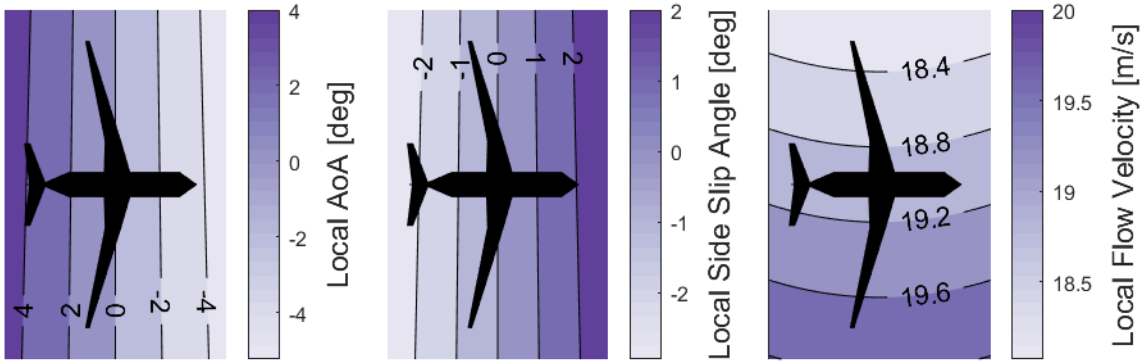

Fig. 8 The variation in the the local angle of attack, side slip angle and velocity magnitude across the planform of the AlbatrossOne model, in the body frame of reference, for a constant-cone-angle manoeuvre, at $\alpha = 0\,\text{deg}$, $\beta = 0\,\text{deg}$, $V = 19ms^{-1}$

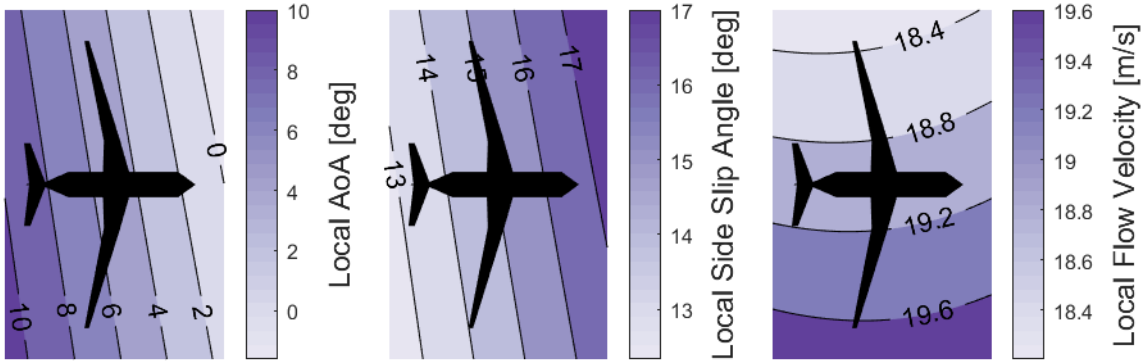

Fig. 9 The variation in the the local angle of attack, side slip angle and velocity magnitude across the planform of the AlbatrossOne model, in the body frame of reference, for a constant-cone-angle manoeuvre, at $\alpha = 5\,\text{deg}$, $\beta = 10\,\text{deg}$, $V = 19ms^{-1}$

B. System Dynamics

To assess the effect of the tether on the dynamics of a UAV, the EoMs derived in section IV were utilised to calculate the modal frequencies and dampings about fixed equilibrium positions. In total, three configurations were used:

1) The free-flight EoM were used, with the UAV in a steady-level-flight condition
2) The tethered EoM were used, with the UAV in a constant-cone-angle manoeuvre configuration
3) The tethered EoM were used, with the UAV in a constant-cone-angle manoeuvre configuration. Additionally, the roll DoF was locked, replicating locking the roll cage on the AlbatrossOne UAV, as shown in Fig.3

In all cases, for a given velocity, the EoM were linearised about the equilibrium position by calculating an estimate of the jacobian matrix, J, using a sixth order accurate numerical differentiation scheme, such that

$$\dot{\vec{x}} = Jx, \qquad \vec{x} = \left[\vec{q}, \dot{\vec{q}}\right]^T \tag{15}$$

The modal frequencies and dampings were then estimated by calculating the eigenvalues and vectors of the jacobian matrix, J. The variation in the eigenvalues for the free-flight case across a range of velocities is shown in the root-locus plot in Fig. 10a in which each mode has been associated with the canonical aircraft dynamic mode it most closely represents. Specific frequencies and dampings can also be found in Tab. 1. This particular model was characterised by an unstable phugoid below 20ms^{-1}, an unstable roll subsidence mode below 23ms^{-1}, and a marginally stable dutch roll mode.

Figure 10b shows a comparison between the eigenvalues of both the free and tethered case, with modes three, four, and five of the tethered case closely resembling the dutch roll, short period and spiral modes of the free case respectively. In particular the spiral mode was generally unaffected by the tether constraint; the short period mode shows the same qualitative trend, albeit less stable in the tethered case; and the dutch roll mode seems to be coupled with the short period mode as it now becomes more stable with velocity.

However, there are significant differences in the first two modes for the tethered and free-free cases. The inclusion of the tether constrains the vertical motion of a UAV, and as such primarily effects the longitudinal modes. In particular, the phugoid mode is significantly affected as it is characterised by an exchange of altitude with velocity. In Fig. 10b the phugoid mode of the free-flight case has transformed into mode two of the tethered case. Mode two is itself analogous to a classical mode of a spherical pendulum, namely Airy's precession [35]. This mode is characterised as an exchange of cone angle and velocity across a cycle, and hence converts a constant-cone-angle, circular orbit, into an inclined elliptical orbit. Airy's precession can be thought of as a constrained phugoid, as the primary mechanism of both modes is an exchange of kinetic and gravitational potential energy. As outlined in ref. [35], and also present in this system, the period of mode two in the tethered case differs from the time taken for a UAV to travel through a polar angle of 360 degrees. As such the inclined elliptical orbit of a UAV will precess around the centre of the tether.

The characteristics of the roll subsidence mode in Fig. 10a are dramatically different then that of mode one in the tethered case. In particular, this new mode is now oscillatory and is destabilised with increasing velocity. This new oscillatory behaviour is due to a coupling between the roll angle of the UAV and the cone angle, as a changing roll angle will change the magnitude of the force acting perpendicular to the tether.

As shown in Fig. 11, by locking the roll DoF, modes associated with this motion either disappear, such as the spiral mode, or are significantly altered, such as the third mode which resembles some form of constrained dutch roll motion. Additionally, the second mode, which is analogous to Airy's precession, is now unstable across all velocities, with a period of around five seconds. Indeed for other aircraft configurations the controllability of this mode may be a key consideration when flying a UAV on a tether.

In conclusion, operating a UAV on a tether, particularly with an unlocked roll cage, can provide a good representation of the lateral stability of a UAV. In the example of the AlbatrossOne UAV there is a distinct mode associated with each of the 5 classical aircraft dynamic modes, with varying levels of correlation, due to the constraints and couplings imposed by the tether. Overall, the repeatable environment provided by the tether provides a good opportunity to both assess the lateral stability of a UAV and to tune a dynamic model to provide greater confidence in the free-flight stability of a UAV.

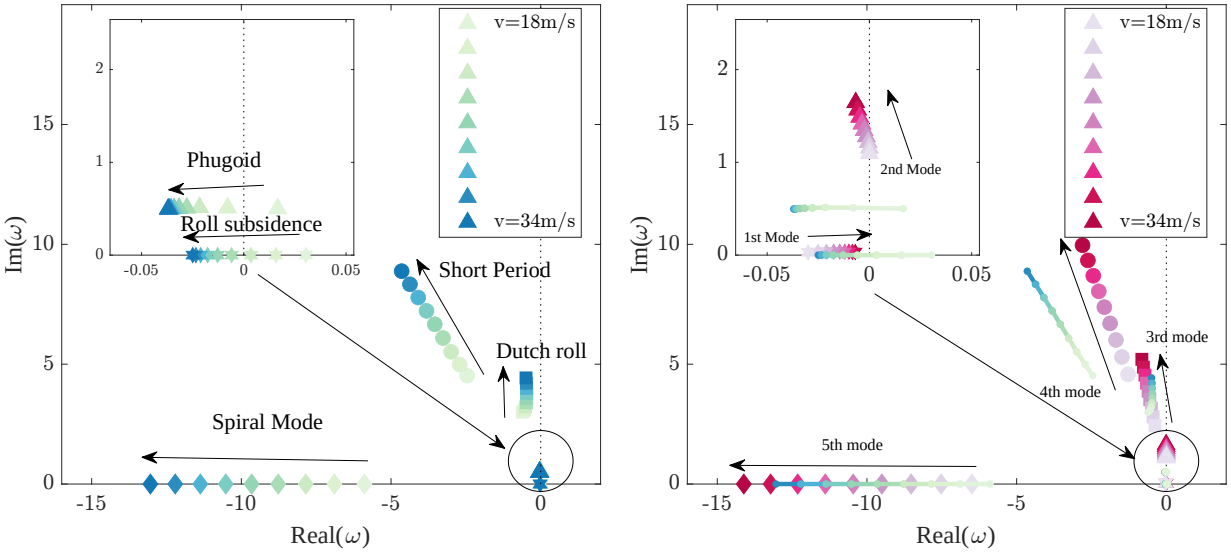

(a) Free flying 6 DoF AlbatrossOne mode stability analysis.

(b) AlbatrossOne mode stability analysis for tether length L = 23 m with roll DoF enabled.

Fig. 10 Stability analysis for the free flying and tethered AlbatrossOne model (tether length L = 23 m). In green the free flying modes.

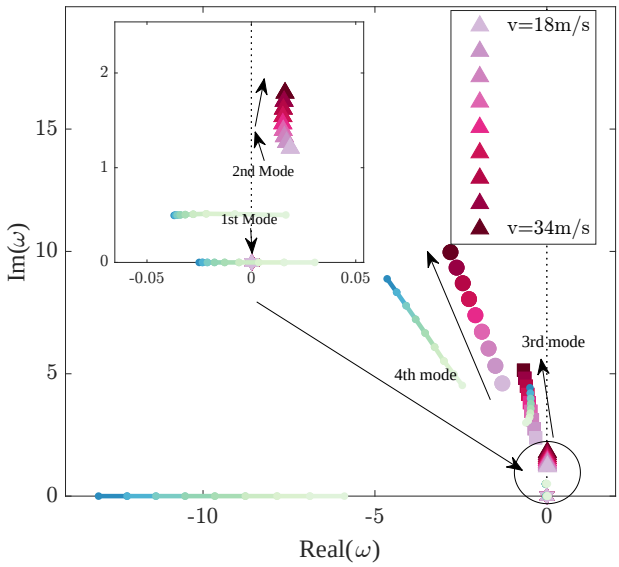

Fig. 11 AlbatrossOne mode stability analysis for tether length L = 23 m with roll DoF locked.

	v=20 m/s		v=26 m/s		v=30 m/s	
	f/τ	ζ	f/τ	ζ	f/τ	ζ
Phugoid	0.08 Hz	0.02	0.08 Hz	0.06	0.08 Hz	0.07
Short period	0.78 Hz	0.47	1.06 Hz	0.47	1.24 Hz	0.46
Dutch roll	0.49 Hz	0.17	0.57 Hz	0.13	0.64 Hz	0.12
Roll subsidence	63 s (U)	-	78 s (S)	-	47 s (S)	-
Spiral	0.14 s (S)	-	0.1 s (S)	-	0.1 s (S)	-

Table 1 AlbatrossOne stability modes properties at three different velocities. f= frequency, τ = time constant for nonoscillatory modes and ζ = damping. (S) = stable, (U) = unstable.

	v=20 m/s		v=26 m/s		v=30 m/s	
	Δf	$\Delta\zeta$	Δf	$\Delta\zeta$	Δf	$\Delta\zeta$
3rd mode (Dutch roll)	-10%	-12%	+8%	+15%	+14%	+25%
4th mode (Short period)	+8%	-42%	+11%	-42%	+12%	-41%

Table 2 Comparison of similar oscillatory modes for the free flying and tethered free roll configurations.

VI. AlbatrossOne Flight Test

This section provides an overview of the results from the tethered testing conducted with the AlbatrossOne model, as described in section III, and is designed as a test case to highlight some of the capabilities of testing a UAV whilst constrained by a tether.

Figure 12 shows a comparison between the cone angle and loading factors predicted using the constant-cone-angle assumption developed in section IV and those of an example flight test of the AlbatrossOne model. In the experimental data the cone angle was approximated using the measured bank angle of the UAVs internal gyroscope. Between a velocity of 5 and 16 ms^{-1} there is a good match between the two data sets, with this region representing the time between launching the model and getting up to the test velocity. Beyond 16 ms^{-1}, a test was conducted in which both the AoA and the side slip angle were varied significantly, and some dynamcis manouvres were conducted, resulting in larger variations of all 3 parameters in Fig. 12. Overall, this figure shows that the equation's derived in section IV provide a good approximation of the achievable flight envelope of a tethered UAV.

One of the primary aims of this test program was to develop an understanding as to how the coast angle of both the left and right folding wingtip (the angle at which the wingtips are statically stable) varied with both AoA and side-slip. To do this the model was flown at a constant speed whilst incrementally varying both the AoA and side-slip angle of the model. This test was repeated for both the FWT32 and FWT37 wingtip configurations, as described in section III. Figure 13 shows an example variation in AoA, side slip and velocity during a test of the FWT32 configuration. The values in Fig. 13 have been corrected for flow curvature effects so that they represent the AoA, side slip angle and velocity at the CoM of the UAV. Each test was flown manually and was limited by the battery capacity of the UAV, therefore it was difficult to maintain a constant velocity across the entire test matrix, with Fig. 13 showing up to a 15% variation in speed across the test.

Figure 15a shows a comparison between the left and right coast angles for both the FWT32 and FWT37 configurations across a range of attitudes. Considering first a side slip angle of zero degrees, increasing the AoA of the UAV increases the lift produced by the wingtips, therefore the coast angle must increase to reduce the local AoA on the wingtip and maintain the same moment about the hinge, as shown experimentally in Fig. 15a. Cheung et al. [24] approximated this change in the local AoA with fold angle as

$$\Delta\alpha = -\arctan\left(\sin\Lambda\sin\theta\right) \tag{16}$$

Therefore if the flare angle of a wingtip was smaller we would expect to see larger coast angles, as a larger fold angle is required to get the same change in local AoA, with the opposite being true for larger flare angles. This variation in the flare angle can also be achieved by changing the side slip angle of the model, with a positive change in side slip increasing the effective flare angle of the starboard wingtip and decreasing it on the port wingtip. For a constant AoA, this would have the effect of reducing the coast angle of the starboard wingtip and increasing it on the port wingtip, as is

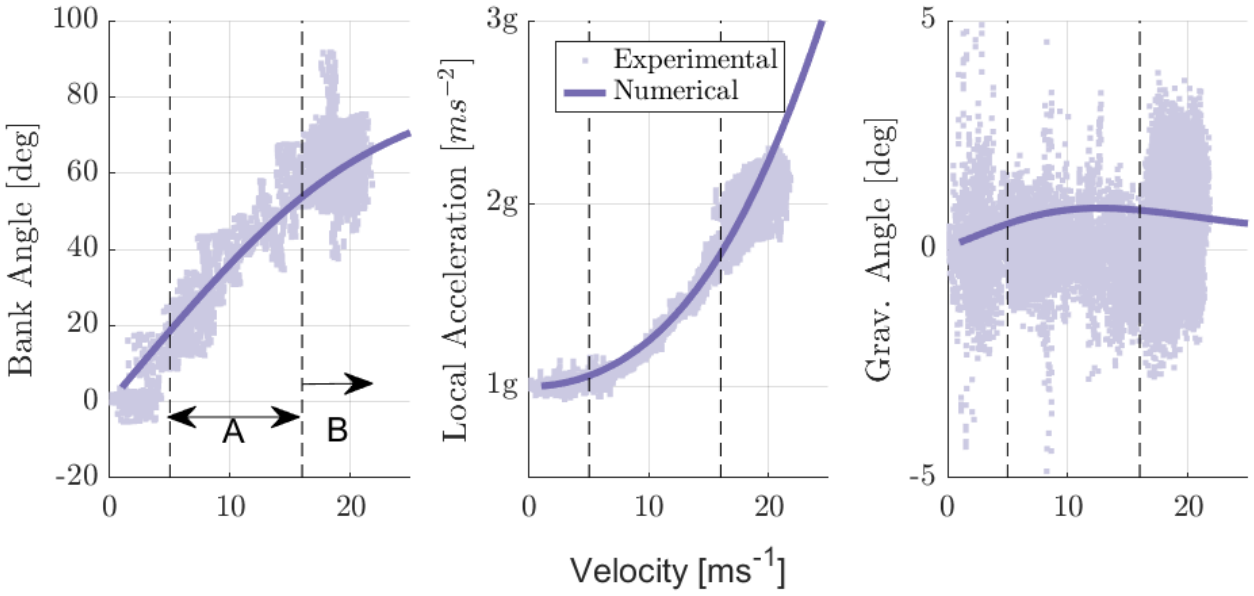

Fig. 12 The variation in the cone angle and load factor predicted with the constant-cone-angle manoeuvre assumption compared with experimental data from an example test of the AlbatrossOne UAV

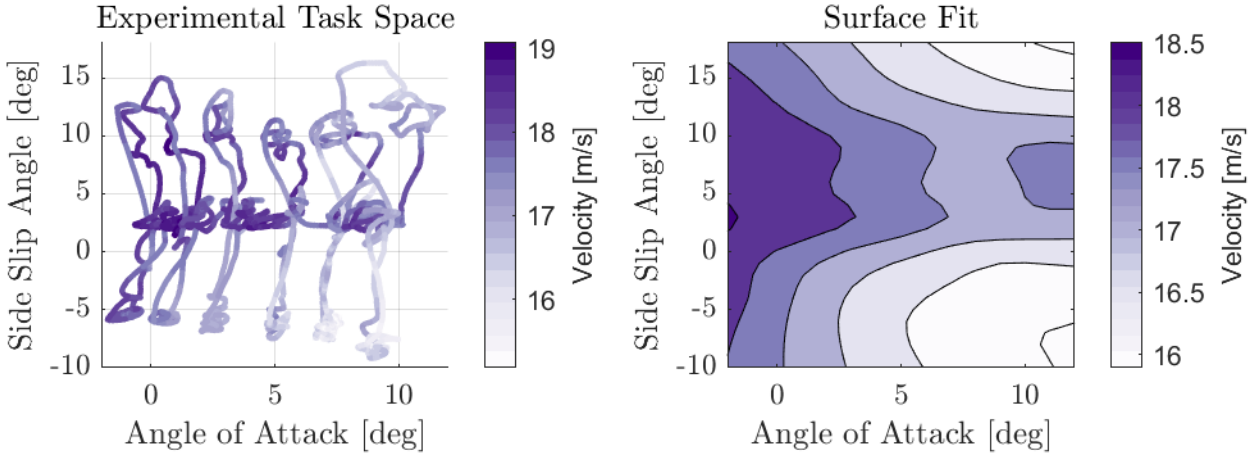

Fig. 13 The variation in AoA, side slip angle and flow speed velocity, during the test programme in the FWT32 configuration

shown experimentally in Fig. 15a. With the opposite also being true for negative side slip angles. Additionally, Fig. 15a shows that the coast angle of the port wingtip is slightly lower than that of the starboard wingtip at zero side-slip, which is due to the varying local velocities experienced by each wingtip.

To model this numerically, the EoM derived in section IV were loosely coupled with an additional EoM for each wingtip

$$m_f \left|\vec{r}_f - \hat{r}_0(\hat{r}_0 \cdot \vec{r}_f)\right|^2 \ddot{\theta}_i = \hat{r}_0 \cdot \left(\sum_{j=1}^{N} \left(\vec{r}_j \times \vec{F}_j \right) + \vec{r}_f \times m_f \vec{a} \right) \tag{17}$$

where: the ith wingtip is modelled as a point mass m_f a displacement r_f away from the hinge line; $\vec{F}_j$ is the force from the jth vortex filament which is a displacement $\vec{r}_j$ from the hinge line and N is the total number of vortex filaments on the wingtip; $\vec{a}$ is the inertial acceleration vector experienced by the ith wingtip; and $\hat{r}_0$ is the unit vector in the direction of the hinge line. All of these terms are defined graphically in Fig. 14.

By first using the process outlined in section IV to calculate the required thrust for a given UAV attitude in a constant-cone-angle manoeuvre, the coast angle of the left and right wingtips can be calculated by finding the fold angle at which the right-hand-side of Eqn. (17) is equal to zero. Note that at each step in this minimisation process the vortex lattice mesh of each wingtip is rotated about the hinge line by the required fold angle, and the aerodynamic influence matrix recalculated. It is also interesting to note that the local acceleration vector, $\vec{a}$, on each wingtip differs due to the differing centripetal accelerations experienced at different locations on the UAV.

This process was completed at a range of AoAs and side slip angles. To account for the varying velocity in the experimental data, the flow velocity at each attitude was calculated using a surface fit of the experimental velocities, such as shown in Fig. 13. Figure 15b shows the resulting numerical variations in coast angle with attitude. These results are qualitatively similar to those measured experimentally, with an increase in side slip angle increasing the coast angle of the port wingtip and reducing it on the starboard wingtip. Additionally there is a smaller variation in coast angles for the FWT37 configuration in both data sets. There are however some key differences between Figs. 15a & 15b. Firstly, at zero side slip angle there is a much larger variation in coast angle with AoA in the experimental data. These differences may indicate that the underlying shape of the wing used in the VLM model may be incorrect, in particular there was significant uncertainty in the twist distribution of the wingtip. Equally, Eqn. (17) does account for any bending or twisting of the inner wing, albeit the AlbatrossOne wing was design to be particularly stiff [32].

Secondly, there is a noticeable kink in the experimental data for both wingtip configurations at around ±5 degrees side slip angle. Beyond this kink the coast angle increases more rapidly towards 90 degrees. This effect is not captured in the numerical model and the cause is currently unclear, although it is presumed to be due to either 3D aerodynamic effects such as stall on the wingtip or fuselage, or a flaw constant-cone-angle assumption, leading to an under prediction of the local side-slip angle on the wingtips.

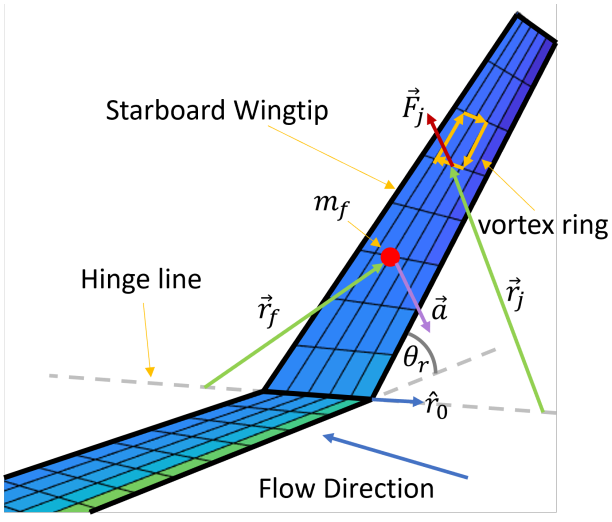

Fig. 14 A graphical representation of the forces acting on a folding wingtip

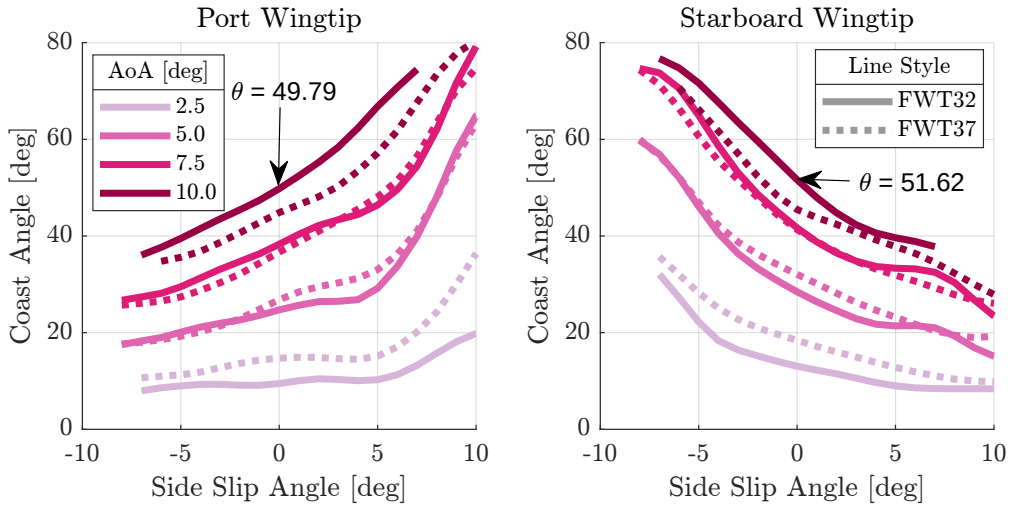

(a) Experimental

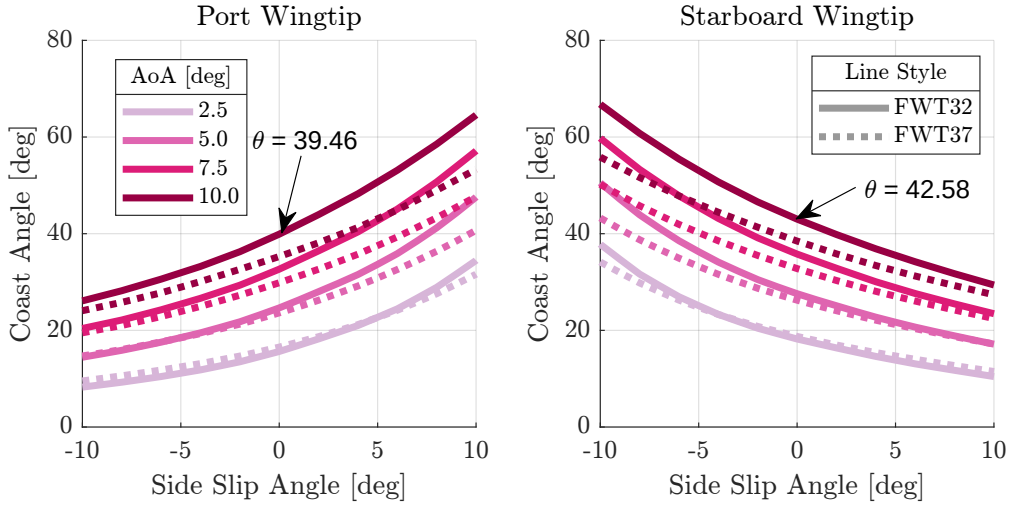

(b) Numerical

Fig. 15 The numerical and experimental variations in left and right coast angles of the AlbatrossOne model with AoA and side slip angle, in multiple configurations

Considering again Eqn. (16), as the flare angle of a wingtip is reduced the relative change in the local AoA with fold angle will also reduce, until at a flare angle of zero degrees there is no change in the local AoA, and the wingtip will become neutrally stable (when ignoring gravitational forces). As you further reduce the flare angle the wingtip will become unstable. Destabilising the wingtip can also be achieved by changing the side slip angle of the aircraft, reducing the effective flare angle of the hinge. The side slip angle at which the wingtip becomes unstable, which will be called beta-critical, is an important property to calculate for a UAV with FFWTs. Conti et al. [36] suggested the beta-critical was equivalent to the flare angle, which is the only current estimation of this value in literature.

In the tests presented in Fig. 15a a mechanical stop had been attached to the wingtips, preventing the fold angle from going above 85 degrees. However, in a later test this 'stop' was removed, allowing the wingtip to fold on top of the inner wing if it became unstable, as shown in Fig. 16 - it seems important to note that conducting such a test with the UAV in free-flight would have most likely ended with its destruction. During this test the starboard wingtip became unstable three times, at an average side slip angle of -8.5 degrees, and the port wingtip became unstable three times, at an average side slip angle of 10.5 degrees. Both of these estimation of the beta-critical angle are significantly below the flare angle of the wingtips (17.5 degrees).

The stability boundary of the numerical model could be predicted by looking at the sign of the derivative of Eqn. (17) with respect to the fold angle. However, beta-critical angles were found to always be close to the flare angle. Therefore, this significant reduction in the beta-critical angle is a topic for further discussion, and is believed to emanate from the same physical phenomena that causes the kink in Fig. 15a, as discussed previously.

More anecdotally, it is envisaged that FFWTs would typically be locked in flight for optimal cruise performance, whilst unlocked during manoeuvres and gust encounters to alter the dynamic behaviour and reduce peak wing loading. Such a system has been integrated into the AlbatrossOne UAV and is the so called Semi-Aeroelastic Hinge (SAH). Flying the UAV on the tether provided a good test environment for such a system, with Fig. 17 showing a time history of the right wingtips fold angle during a wingtip "release and recovery". By testing such a system on the tether the effect on the aircraft's dynamics could be assessed, as well as failure conditions, such as if only one wingtip was released. Overall, testing a UAV whilst constrained to a tether provided a good environment for testing system integration, at the level of the entire UAV, in a safe and controlled manner. Indeed, the last test conducted with the AlbatrossOne model was of the parachute recovery system, giving the the team confidence if this system was ever required in a free-flight scenario.

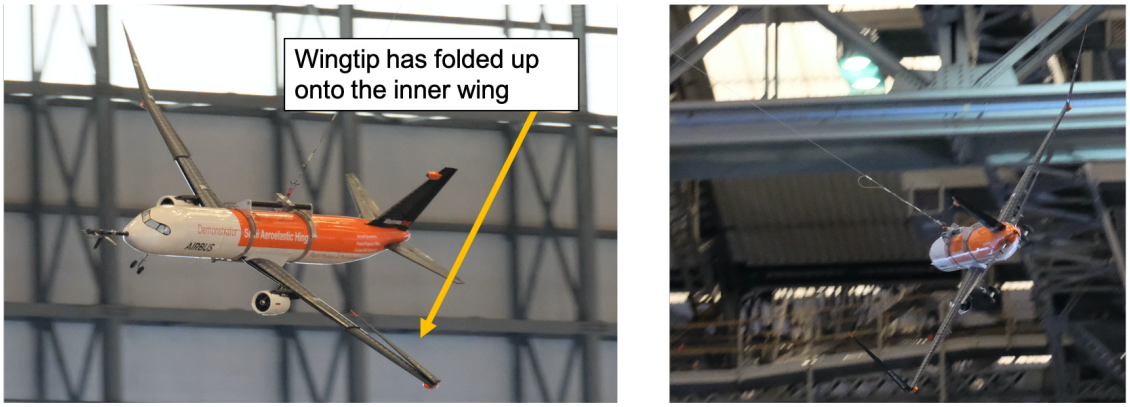

Fig. 16 Images of the UAV at large side-slip angles, with and without a mechanical stop of the wingtips. Copyright ©2021 Airbus

Fig. 17 Typical time history of the right wingtip during a release and retrieval

VII. Conclusions

This paper presents a novel method for testing a Unmanned Aerial Vehicle (UAV) by constraining it motion by use of a tether, resulting in controlled cyclic and elliptical flight paths. The Equations of Motion (EoM) of a simplified, five Degrees of Freedom (DoF), model of this system are derived herein. The EoM are then used to characterise the static and dynamic testing capabilities of such a rig, with a particular focus on: a constant-cone-angle manoeuvre in which the height of the UAV remains constant whilst flight parameters such as the Angle of Attack (AoA) and side slip angle can be varied independently; how the tether changes the dynamic response of the UAV and how this relates to the free-flight modes. Results from such an experiment with the AlbatrossOne UAV are also presented, which aimed to use this novel testing method to characterise the effect of side slip on the equilibrium position of free floating hinged wingtips, with good correlation found between both experimental and numerical predictions, and experimentally push the boundaries of the flight envelop to verify the stability boundary of such a device. Conducting such testing in a free-flight condition would risk destroying the aircraft, and as such tethered flight testing is presented as an attracted alternative or complement to more traditional techniques of testing UAVs.

Appendix A: Full Form of the Equations of Motion of a Tethered Aircraft

As detailed in section IV the final form of the EoM of an aircraft constrained by a tether are

$$\mathbf{M}\left(\mathbf{q},\dot{\mathbf{q}}\right)\ddot{\mathbf{q}} - \vec{f}\left(\mathbf{q},\dot{\mathbf{q}}\right) = \vec{g}\left(\mathbf{q},\dot{\mathbf{q}}\right) \tag{18}$$

where the mass matrix, $\mathbf{M}$, is defined as

$$\begin{bmatrix} h^2 m \sin^2(\sigma) & 0 & 0 & 0 & 0 \\ 0 & h^2 m & 0 & 0 & 0 \\ 0 & 0 & M_{33} & -I_{yy}\sin(\beta) & M_{35} \\ 0 & 0 & -I_{yy}\sin(\beta) & I_{yy} & 0 \\ 0 & 0 & M_{35} & 0 & I_{xx}\sin^2(\alpha) + I_{zz}\cos^2(\alpha) \end{bmatrix} \tag{19}$$

where

$$M_{33} = I_{xx}\cos^2(\alpha)\cos^2(\beta) + I_{yy}\sin^2(\beta) + I_{zz}\sin^2(\alpha)\cos^2(\beta) \tag{20}$$

$$M_{35} = \frac{\left(-I_{xx} + I_{zz}\right)\left(\sin(2\alpha - \beta) + \sin(2\alpha + \beta)\right)}{4} \tag{21}$$

the conservative force vector, $\vec{f}$, is defined as

$$\begin{bmatrix} h^2 m \sin(2\sigma)\dot{\sigma}\dot{\xi} \\ hm\left(g - h\cos(\sigma)\dot{\xi}^2\right)\sin(\sigma) \\ 0 \\ 0 \\ 0 \end{bmatrix} \tag{22}$$

and the external force vector, $\vec{g}$ is defined as

$$\begin{bmatrix} h\left(-Y\sin(\beta) + Z\sin(\alpha)\cos(\beta) + (X+\tau)\cos(\alpha)\cos(\beta)\right)\sin(\sigma) \\ g_2 \\ L\cos(\alpha)\cos(\beta) - M\sin(\beta) + N\sin(\alpha)\cos(\beta) \\ M \\ -L\sin(\alpha) + N\cos(\alpha) \end{bmatrix} \tag{23}$$

where

$$g_2 = -L\cos(\alpha)\cos(\beta) + M\sin(\beta) - N\sin(\alpha)\cos(\beta) \tag{24}$$

$$+ h\left(Y\cos(\beta)\cos(\mu) + Z\left(\sin(\alpha)\sin(\beta)\cos(\mu) - \sin(\mu)\cos(\alpha)\right)\right) \tag{25}$$

$$+ h\left((X+\tau)\left(\sin(\alpha)\sin(\mu) + \sin(\beta)\cos(\alpha)\cos(\mu)\right)\right) \tag{26}$$

Appendix B: Derivation of the Body Velocity of a Constrained UAV

Given the generalised coordinates, $\vec{q}$, for a UAV constrained by a tether

$$\vec{q} = \left[\xi, \sigma, \mu, \beta, \phi\right]^T \tag{27}$$

and the definition of the 4x4 homogeneous transformation matrix

$$\mathbf{H}_a b = \begin{bmatrix} \mathbf{R}_{ab} & \vec{p}_{ab} \\ \vec{0} & 1 \end{bmatrix} \tag{28}$$

which describes the transformation from reference frame a to reference frame b by first translating the origin by the 3x1 vector $\vec{p}_{ab}$, and then rotating the coordinate system by the 3x3 rotation matrix $\mathbf{R}_{ab}$. The homogeneous transformation matrix between the spatial frame and the tether frame of reference can be defined as

$$\mathbf{H}_{st} = H_{Rz}(\xi)H_{Rx}(\pi - \sigma)T(0, 0, h) \tag{29}$$

where $H_{Rn}(m)$ represent the homogeneous transform for the rotation about the n'th axis in the anticlockwise direction by an angle of m radians, and $T(x, y, z)$ represents the homogeneous transform for a translation by x, y and z along there respective axes. Furthermore, the transformation matrix between the spatial frame and the body frame can be defined as

$$\mathbf{H}_{sb} = \mathbf{H}_{st}H_{Rx}(\mu)H_{Rz}(\beta)H_{Ry}(\alpha)T(x, y, z) \tag{30}$$

The local velocity of a point $\vec{x}_b$ in the body frame of reference can then be calculated using the notion of the *body velocity*, $\hat{V}^b_{sb}$ [37]

$$\vec{v}_{xb} = \hat{V}^b_{sb}\vec{x}_b = \mathbf{H}^{-1}_{sb}\dot{\mathbf{H}}_{sb}\vec{x}_b \tag{31}$$

Acknowledgments

The first author is supported via an Engineering and Physical Science Research Council (EPSRC) iCASE award (19000004) sponsored by Airbus Operations UK Ltd.

References

[1] Barbarino, S., Bilgen, O., Ajaj, R., Friswell, M., and Inman, D., "A Review of Morphing Aircraft," *Journal of Intelligent Material Systems and Structures - J INTEL MAT SYST STRUCT*, Vol. 22, 2011. https://doi.org/10.1177/1045389X11414084.

[2] Li, D., Zhao, S., Da Ronch, A., Xiang, J., Drofelnik, J., Li, Y., Zhang, L., Wu, Y., Kintscher, M., Monner, H. P., Rudenko, A., Guo, S., Yin, W., Kirn, J., Storm, S., and Breuker, R. D., "A Review of Modelling and Analysis of Morphing Wings," *Progress in Aerospace Sciences*, Vol. 100, 2018, pp. 46–62. https://doi.org/10.1016/j.paerosci.2018.06.002.

[3] Huang, M., and Wang, Z.-W., "A Review of Wind Tunnel Based Virtual Flight Testing Techniques for Evaluation of Flight Control Systems," *International Journal of Aerospace Engineering*, Vol. 2015, 2015, pp. 1–22. https://doi.org/10.1155/2015/672423.

[4] Noll, T. E., Brown, J. M., Perez-Davis, M. E., Ishmael, S. D., Tiffany, G. C., and Gaier, M., "Investigation of the Helios Prototype Aircraft Mishap," Tech. rep., NASA, 2004. URL https://www.nasa.gov/pdf/64317main_helios.pdf[retrieved1stJune2021].

[5] Williams, P., Lansdorp, B., and Ockesl, W., "Optimal Crosswind Towing and Power Generation with Tethered Kites," *Journal of Guidance, Control, and Dynamics*, Vol. 31, 2008, pp. 81–93. https://doi.org/10.2514/1.30089.

[6] Williams, P., "Optimal wind power extraction with a tethered kite," *Collection of Technical Papers - AIAA Guidance, Navigation, and Control Conference 2006*, Vol. 2, 2006, pp. 1167–1195. https://doi.org/10.2514/6.2006-6193.

[7] Terink, E. J., Breukels, J., Schmehl, R., and Ockels, W. J., "Flight dynamics and stability of a tethered inflatable kiteplane," *Journal of Aircraft*, Vol. 48, 2011, pp. 503–513. https://doi.org/10.2514/1.C031108.

[8] Williams, P., Lansdorp, B., and Ockels, W., "Flexible tethered kite with moveable attachment points, part I: Dynamics and control," *Collection of Technical Papers - 2007 AIAA Atmospheric Flight Mechanics Conference*, Vol. 2, 2007, pp. 994–1017. https://doi.org/10.2514/6.2007-6628.

[9] Williams, P., Lansdorp, B., and Ockels, W., "Nonlinear control and estimation of a tethered kite in changing wind conditions," *Journal of Guidance, Control, and Dynamics*, Vol. 31, 2008, pp. 793–798. https://doi.org/10.2514/1.31604.

[10] Bourdin, P., Gatto, A., and Friswell, M. I., "Aircraft Control Via Variable Cant-Angle Winglets," *Journal of Aircraft*, Vol. 45, No. 2, 2008, pp. 414–423. https://doi.org/10.2514/1.27720.

[11] Mills, J., and Ajaj, R., "Flight Dynamics and Control Using Folding Wingtips: An Experimental Study," *Aerospace*, Vol. 4, No. 2, 2017, p. 19. https://doi.org/10.3390/aerospace4020019.

[12] Gatto, A., Bourdin, P., and Friswell, M. I., "Experimental Investigation into the Control and Load Alleviation Capabilities of Articulated Winglets," *International Journal of Aerospace Engineering*, Vol. 2012, 2012, pp. 1–15. https://doi.org/10.1155/2012/789501.

[13] Guerrero, J., Sanguineti, M., and Wittkowski, K., "Cfd Study of the Impact of Variable Cant Angle Winglets on Total Drag Reduction," *Aerospace*, Vol. 5, No. 4, 2018, p. 126. https://doi.org/10.3390/aerospace5040126.

[14] Daniele, E., De Fenza, A., and Vecchia, P., "Conceptual Adaptive Wing-Tip Design for Pollution Reductions," *Journal of Intelligent Material Systems and Structures - J INTEL MAT SYST STRUCT*, Vol. 23, 2012, pp. 1197–1212. https://doi.org/10.1177/1045389X12445030.

[15] Wang, C., Khodaparast, H., Friswell, M., Shaw, A., Xia, Y., and Walters, P., "Development of a Morphing Wingtip Based on Compliant Structures," *Journal of Intelligent Material Systems and Structures*, 2018, p. 1045389X1878307. https://doi.org/10.1177/1045389X18783076.

[16] Wang, C., Khodaparast, H. H., and Friswell, M. I., "Conceptual Study of a Morphing Winglet Based on Unsymmetrical Stiffness," *Aerospace Science and Technology*, Vol. 58, 2016, pp. 546–558. https://doi.org/10.1016/j.ast.2016.09.015.

[17] Castrichini, A., Hodigere Siddaramaiah, V., Calderon, D. E., Cooper, J. E., Wilson, T., and Lemmens, Y., "Nonlinear Folding Wing Tips for Gust Loads Alleviation," *Journal of Aircraft*, Vol. 53, No. 5, 2016, pp. 1391–1399. https://doi.org/10.2514/1.c033474.

[18] Cheung, R. C. M., Rezgui, D., Cooper, J. E., and Wilson, T., "Testing of a Hinged Wingtip Device for Gust Loads Alleviation," *Journal of Aircraft*, Vol. 55, No. 5, 2018, pp. 2050–2067. https://doi.org/10.2514/1.c034811.

[19] Castrichini, A., Siddaramaiah, V. H., Calderon, D. E., Cooper, J. E., Wilson, T., and Lemmens, Y., "Preliminary Investigation of Use of Flexible Folding Wing Tips for Static and Dynamic Load Alleviation," *The Aeronautical Journal*, Vol. 121, No. 1235, 2017, pp. 73–94. https://doi.org/10.1017/aer.2016.108.

[20] Castrichini, A., Wilson, T., Saltari, F., Mastroddi, F., Viceconti, N., and Cooper, J., "Aeroelastics Flight Dynamics Coupling Effects of the Semi-Aeroelastic Hinge Device," *Journal of Aircraft*, 2019, pp. 1–9. https://doi.org/10.2514/1.C035602.

[21] Cheung, R. C., Rezgui, D., Cooper, J. E., and Wilson, T., *Testing of Folding Wing-Tip for Gust Load Alleviation in High Aspect Ratio Wing*, San Diego, California, 2019. https://doi.org/10.2514/6.2019-1863.

[22] Bradley, M. K., Droney, C. K., and Allen, T. J., "Subsonic Ultra Green Aircraft Research. Phase Ii-Volume I; Truss Braced Wing Design Exploration,," Tech. Rep. CR-2015-218704, NASA, 2015. URL https://ntrs.nasa.gov/citations/20150017036.

[23] Anon, *Annex 14*, 8th ed., Aerodromes, Vol. 1, International Civil Aviation Orginization, Montréal, Quebec, 2018.

[24] Cheung, R. C. M., Rezgui, D., Cooper, J. E., and Wilson, T., "Testing of Folding Wingtip for Gust Load Alleviation of Flexible High-Aspect-Ratio Wing," *Journal of Aircraft*, 2020, pp. 1–13. https://doi.org/10.2514/1.c035732.

[25] Balatti, D., Haddad Khodaparast, H., Friswell, M. I., Manolesos, M., and Amoozgar, M., "The Effect of Folding Wingtips on the Worst-Case Gust Loads of a Simplified Aircraft Model," *Proceedings of the Institution of Mechanical Engineers, Part G: Journal of Aerospace Engineering*, 2021. https://doi.org/10.1177/09544100211010915.

[26] Dussart, G., Yusuf, S., and Lone, M., "Identification of in-Flight Wingtip Folding Effects on the Roll Characteristics of a Flexible Aircraft," *Aerospace*, Vol. 6, No. 6, 2019, p. 63. https://doi.org/10.3390/aerospace6060063.

[27] Wilson, T., Castrichini, A., Azabal, A., Cooper, J., Ajaj, R., and Herring, M., *Aeroelastic Behaviour of Hinged Wing Tips*, 2017. URL www.asdjournal.org/public/Proceedings/IFASD_2017/IFASD-2017-216.pdf.

[28] Healy, F., Cheung, R. C., Neofet, T., Lowenberg, M. H., Rezgui, D., Cooper, J. E., Castrichini, A., and Wilson, T., "Folding Wingtips for Improved Roll Performance," AIAA Scitech 2021 Forum, 2021. https://doi.org/10.2514/6.2021-1153, URL https://doi.org/10.2514/6.2021-1153.

[29] Healy, F., Cheung, R., Rezgui, D., and Cooper, J., "(Unpublished) Nonlinear Geometric Considerations for Flared Folding Wingtips," Submitted to AIAA Scitech Forum 2022, 2022.

[30] Wilson, T., Castrichini, A., Paterson, J., and Arribas Ardura, R., "Non-Linear Aeroelastic Behaviour of Hinged Wing Tips," 6th Aircraft Structural Design Conference, We The Curious, Bristol, UK, 2018. https://doi.org/10.2514/6.2017-0502.

[31] Healy, F., Cheung, R., Neofet, T., Lowenberg, M., Rezgui, D., Cooper, J., Castrichini, A., and Wilson, T., "Folding Wingtips for Improved Roll Performance," *Journal of Aircraft*, 2021, pp. 1–14. https://doi.org/10.2514/1.C036372.

[32] Wilson, T., Kirk, J., Hobday, J., and Castrichini, A., "Small Scale Flying Demonstration of Semi Aeroelastic Hinged Wing Tips," International Forum on Aeroelasticity and Structural Dynamics, Savannah, Georgia, USA, 2019. URL www.asdjournal.org/public/Proceedings/IFASD_2019/IFASD-2019-076.pdf.

[33] Meurer, A., Smith, C. P., Paprocki, M., Certík, O., Kirpichev, S. B., Rocklin, M., Kumar, A., Ivanov, S., Moore, J. K., Singh, S., Rathnayake, T., Vig, S., Granger, B. E., Muller, R. P., Bonazzi, F., Gupta, H., Vats, S., Johansson, F., Pedregosa, F., Curry, M. J., Terrel, A. R., Roucka, S., Saboo, A., Fernando, I., Kulal, S., Cimrman, R., and Scopatz, A., "Sympy: Symbolic Computing in Python," *PeerJ Computer Science*, Vol. 3, 2017, p. e103. https://doi.org/10.7717/peerj-cs.103.

[34] Katz, J., and Plotkin, A., *Low-Speed Aerodynamics*, 2nd ed., Cambridge Aerospace Series, Cambridge University Press, Cambridge, 2001. https://doi.org/10.1017/CBO9780511810329, URL https://www.cambridge.org/core/books/lowspeed-aerodynamics/077FAF851C4582F1B7593809752C44AE.

[35] Airy, G. B., "On the Vibration of a Free Pendulum in an Oval Differing Little from a Straight Line," *Memoirs of the Royal Astronomical Society*, Vol. 20, 1851, p. 121.

[36] Conti, C., Saltari, F., Mastroddi, F., Wilson, T., and Castrichini, A., "Quasi-Steady Aeroelastic Analysis of the Semi-Aeroelastic Hinge Including Geometric Nonlinearities," *Journal of Aircraft*, 2021, pp. 1–11. https://doi.org/10.2514/1.C036115.

[37] Murray, R. M., *A Mathematical Introduction to Robotic Manipulation*, 1st ed., Routledge, Boca Raton, 1994.